PCCP

PAPER

View Article Online
View Journal | View Issue

Check for updates

Cite this: *Phys. Chem. Chem. Phys.*, 2019, **21**, 16505

Inner-shell X-ray absorption spectra of the cationic series NH_y^+ (y = 0–3)

Sadia Bari,†*[a] Ludger Inhester,†[bc] Kaja Schubert,[ad] Karolin Mertens,[d] Jan O. Schunck,[ad] Simon Dörner,[a] Sascha Deinert,[a] Lucas Schwob,[a] Stefan Schippers,[e] Alfred Müller,[f] Stephan Klumpp[a] and Michael Martins[d]

Received 20th May 2019,
Accepted 2nd July 2019

DOI: 10.1039/c9cp02864a

rsc.li/pccp

Ion yields following X-ray absorption of the cationic series NH_y^+ (y = 0–3) were measured to identify the characteristic absorption resonances in the energy range of the atomic nitrogen K-edge. Significant changes in the position of the absorption resonances were observed depending on the number of hydrogen atoms bound to the central nitrogen atom. Configuration interaction (CI) calculations were performed to obtain line assignments in the frame of molecular group theory. To validate the calculations, our assignment for the atomic cation N^+, measured as a reference, was compared with published theoretical and experimental data.

Open Access Article. Published on 22 July 2019. Downloaded on 2/20/2026 10:19:23 AM.
This article is licensed under a Creative Commons Attribution 3.0 Unported Licence.

Introduction

To understand the function of large biomolecules, like amino acids and peptides, one has to study the properties of their fundamental constituents, *i.e.* their electronic and geometric structure,[1–4] as well as their dynamics.[5–7] By exploiting the element specificity of inner-shell excitation, X-ray absorption spectroscopy (XAS) is an ideal tool to study the local electronic and geometric structure in the vicinity of a specific element within a molecule. Because of the rather large number of atoms within a biomolecule, photoabsoprtion spectra can be complex and sophisticated calculations are needed for their interpretation.[8]

Thus, modelling accurate X-ray absorption spectra for biomolecules is very challenging.[9,10] Instead of addressing an entire biomolecule, one can interpret the (measured) X-ray absorption spectrum as being composed of the contributions of smaller constituents or building blocks of larger molecules. For example, glycine (NH_2–CH_2–COOH), the simplest amino acid, connects the amino group NH_2 and the carboxyl group COOH *via* a methylene bridge. Solved in water, like all amino acids, glycine is a zwitterion composed of a protonated amino group R–NH_2^+ and a de-protonated carboxylic acid COO^- at its iso-electric point. Based on the assumption that the X-ray absorption is dominantly determined by the local chemical environment, knowing the XAS of NH_2^+ and COO^- will facilitate the interpretation of more complicated XAS of *e.g.* glycine.

An inherent difficulty of this approach is that both of these building blocks of glycine are transient ionic molecules which are (almost) impossible to prepare as a solid or as a solution in water. However, an ion beam arrangement can be used to deliver ionic samples to the X-ray interaction region to address their absorption spectrum.[11–15] Mass spectroscopy with high resolving power does not only offer the possibility to prepare a pure, transient molecular ion beam, but additionally provides control about the chemical environment of the molecular ion, enabling or disabling the interaction of chosen elements within the molecule (see Fig. 1). Depending on the number y of hydrogen atoms bound to the central nitrogen atom in NH_y^+, the electronic structure of the respective molecular ion and hence its absorption features will change. Especially inner-shell resonances, like the nitrogen 1s–2p resonances, are sensitive to the chemical environment of a molecule (see *e.g.* ref. 16–18), enabling us to probe the changes in the electronic structure of the respective molecular ions by performing a XAS-experiment.

Whereas there is plenty of previous work on the neutral species of the series NH_y,[19–30] little work on the cations NH_y^+ (y = 1–3) has been published. Theoretical work on the electronic structure of NH^+ [31,32] and NH_2^+ [33] has been done calculating molecular potential curves and bonding angles. Experiments on molecular ions addressed the valence electronic structure of NH_2^+ using VUV photoionisation[34] or the determination of the

[a] *Deutsches Elektronen-Synchrotron (DESY), Notkestr. 85, 22607 Hamburg, Germany. E-mail: sadia.bari@desy.de; Fax: +49 040 8998 4475; Tel: +49 040 8998 5093*
[b] *Center for Free-Electron Laser Science (CFEL), DESY, Notkestr. 85, 22607 Hamburg, Germany*
[c] *The Hamburg Centre for Ultrafast Imaging (CUI), Luruper Chaussee 149, 22761 Hamburg, Germany*
[d] *Department Physik, Universität Hamburg, Luruper Chaussee 149, 22761 Hamburg, Germany. E-mail: michael.martins@desy.de*
[e] *Justus-Liebig-Universität Gießen, I. Physikalisches Institut, Heinrich-Buff-Ring 16, 35392 Gießen, Germany*
[f] *Justus-Liebig-Universität Gießen, Institut für Atom- und Molekülphysik, 35392 Gießen, Germany*
† These authors contributed equally to this work.

Open Access Article. Published on 22 July 2019. Downloaded on 2/20/2026 10:19:23 AM.
This article is licensed under a Creative Commons Attribution 3.0 Unported Licence.

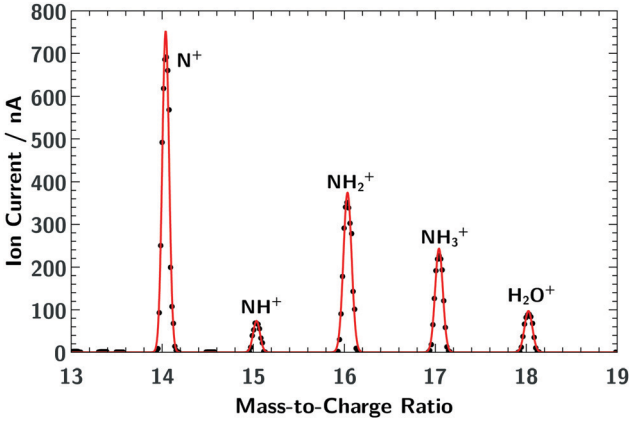

Fig. 1 Mass spectrum of the molecular cation series of NH_y^+ (y = 0–3) showing clearly separated mass lines.

absolute cross section of NH^+ using electron impact ionisation.[35] Yet, there is no detailed information available on the inner-shell XAS of the cationic series NH_y^+ apart from the atomic cation, N^+, which has been studied previously by Gharaibeh *et al.*[36]

Furthermore, the role of NH_y with different numbers y of hydrogen atoms has recently been studied in the liquid phase by Ekimova *et al.* for alkylamines in different solutions.[37,38] They show a strong dependence of the N 1s X-ray spectra on the number y of H atoms and the solution itself.

Here, we report on our systematic investigations on the X-ray absorption for the cationic series NH_y^+ (y = 0–3) in a combined experimental and theoretical work.

Experiment

The PIPE merged-beams set-up[39,40] at the XUV beamline P04[41] of PETRA III, DESY, was used to record XAS spectra of NH_y^+ in the photon energy range of the nitrogen K-edge. Details of the preparation of a molecular ion beam at PIPE have been given in a previous publication.[42]

As primary source for the production of the target molecular cations we have used gaseous NH_3. The gas leaked into the plasma chamber of a 10 GHz Electron Cyclotron Resonance (ECR)[43] ion source *via* an electronic needle valve keeping the gas pressure in the order of 2×10^{-5} hPa.

Fig. 1 shows the mass spectrum of the molecular cation series of NH_y^+ (y = 0–3). As can be seen, the resolving power of the preparation dipole-magnet mass spectrometer is sufficient to distinguish each single ion of the series. Both elements, nitrogen and hydrogen, have two naturally stable isotopes but the abundance ratio for both cases, $^{14}N/^{15}N$ and $^{1}H/^{2}H$, is in the order of 0.99/0.01.[44] Thus, the composition of the mass lines in Fig. 1 can be considered to be almost pure. A possible NH_4^+ molecular ion has the same mass-to-charge ratio as H_2O^+. However, the corresponding absorption spectrum did not show any nitrogen resonances, indicating that no NH_4^+ molecular ions were produced in our ion source.

A beam of singly charged molecular ions was prepared and accelerated to 6 keV kinetic energy, transported to the interaction region on ground potential and collinearly overlapped with the X-ray photons of P04 along an effective absorption length of 1.7 m. The vacuum chamber base pressure of the interaction region was in the order of 1×10^{-9} hPa.

At the nitrogen K-edge, the X-ray photons create an inner-shell hole in the ionic target which results in subsequent Auger decay. The excitation and ionisation is accompanied by possible shake-off processes and is followed by dissociation producing N^{q+} (q = 2, 3) ions. These ions were separated from the target ionic beam with a second magnetic-dipole mass spectrometer. The N^{q+} (q = 2, 3) ions have been counted with a channeltron as a function of the photon energy.

The yield of photoexcited ions of an atomic nitrogen ion N^+ target was measured as a reference to help identifying the spectroscopic features for the molecular targets, as recently done for IH^+.[42] The X-ray photons delivered by the P04 beamline of PETRA III were dispersed by a 400 lines per mm variable line spacing grating (VLS) favouring high photon flux in the order of 1×10^{12} photons per s to 7.5×10^{13} photons per s for monochromator exit slits from 20 μm to 1500 μm. The molecular ion yields were measured with a monochromator exit slit of 500 μm and for the atomic ion yield a slit width of 50 μm was chosen. This results in an energy bandwidth in the order of ΔE = 0.5 eV for the molecular spectra and ΔE = 0.05 eV for the atomic spectrum. The energy axis of the P04 monochromator was calibrated with the known resonance positions of the atomic N^+ 1s → 2p resonance group[36] (see Fig. 3a). The resulting uncertainty of the experimental photon-energy scale is estimated to be approximately 0.1 eV.

Theory details

To assign the observed ion yield peaks with X-ray absorption resonances, we have conducted X-ray absorption cross section calculations with the XMOLECULE toolkit.[45,46] The calculations are based on geometries obtained from geometry optimisation for the respective NH_y^+ cationic ground state using GAMESS[47] on the ROHF/MP2 level employing a 6-311G(d,p) basis set.[48] We have calculated the orientation-averaged X-ray absorption cross section,

$$\sigma = \frac{4}{3}\pi^2\omega\alpha\sum_{r}^{x,y,z}|\langle\psi_i|r|\psi_f\rangle|^2\delta(\omega - E_{photon}), \quad (1)$$

where in eqn (1) $\omega = E_f - E_i$ and $|\psi_i\rangle$, $|\psi_f\rangle$ are the initial and final electronic states with energies E_i and E_f, respectively. The quantity $\langle\psi_i|r|\psi_f\rangle$ is the transition dipole matrix element between the initial and final electronic state, $\alpha \simeq 1/137$ is the fine structure constant, and $\hbar = 1$. For NH_3^+ and NH_2^+, the initial cationic states, $|\psi_i\rangle$, were described with orbitals obtained from a single-configuration-restricted open-shell Hartree–Fock procedure. The initial states $|\psi_i\rangle$ for NH^+ and N^+ have been described based on a complete active space self-consistent field calculation with an active space constructed by the 3σ and the two

 This journal is © the Owner Societies 2019

Open Access Article. Published on 22 July 2019. Downloaded on 2/20/2026 10:19:23 AM.
This article is licensed under a Creative Commons Attribution 3.0 Unported Licence.

π orbitals for NH^+ and the three atomic 2p orbitals for N^+, respectively. These calculations are part of a new implementation in the XMOLECULE toolkit. The final states $|\psi_f\rangle$ in eqn (1) were described in a configuration interaction (CI) calculation employing the same orbitals as for the cationic initial state. The CI calculations included all configurations that are constructed from the cationic reference configurations by promoting a single electron from the K shell to an unoccupied orbital. Moreover, further configurations were included involving an additional excitations of the valence electrons into virtual/singly occupied orbitals. The calculations were conducted using spin- and symmetry-adapted configuration state functions employing the respective discrete point symmetry of the molecule. In cases where the point symmetry of the molecule is not discrete (*e.g.* D_{3h}) the irreducible representation of respective states was identified *via* post-processing of the calculated results. For all the X-ray absorption calculation we used a 6-311G basis set augmented with additional 6 diffuse basis functions of angular momentum s, p, and d, respectively, according to the recipe of Kaufmann *et al.*[49] For efficient integral evaluation XMOLECULE employs the libcint library.[50] Although the employed basis set contains many diffuse functions, it becomes insufficient for very high valence excitations approaching the electronic continuum. Therefore, the agreement with experimental spectra is expected to decrease with higher X-ray excitation energies. Apart from this discrepancy there is a certain imbalance in the description of initial and final electronic states. This imbalance leads to a calculated transition energy which is slightly too low. Thus, we obtain calculated X-ray absorption lines that have lower energies by 1 eV to 2 eV compared to the experimental data. For better comparison between experimental and theoretical results, we have shifted the calculated absorption lines to higher values, as specified in detail within the results section. In particular, we find that for all molecules the photon-energy range $E_{ph} > 405$ eV involves a slightly smaller energy shift compared to $E_{ph} < 405$ eV. Furthermore, the applied shift slightly varies along the series NH_y^+ (y = 0–3). We attribute this varying relative shift to slight differenences in the orbital relaxation of the different molecules and respective excitation ranges.

A similar approach for calculating X-ray absorption spectra has been employed in earlier works[51,52] but with a slightly different configurational space. The mentioned energy shift relative to the experimental data could potentially be avoided by using an orbital set for the final core excited state that has been optimised in the presence of the core hole and might result in an improved modelling of core-hole relaxation effects. However, the calculation of electronic transitions (eqn (1)) becomes computationally very demanding with different orbital sets for initial and final state in combination with a large configuration space. We think that the resulting energy shift of 1 eV to 2 eV is acceptable for the purposes of our study and therefore decided keep a common orbital set.

Results and discussion

The normalised ion yields Y measured for the target ion series NH_y^+ (y = 0–3) are shown in Fig. 2 from y = 0 (panel a) to y = 3 (panel d).

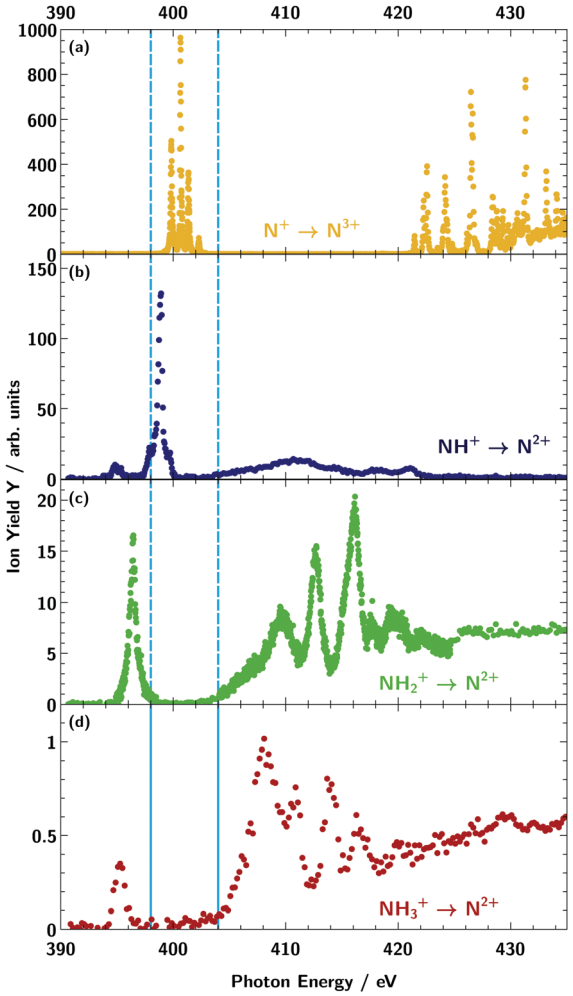

Fig. 2 Product ion yields Y (see eqn (2)) from photoionisation and/or photofragmentation of the target ion series NH_y^+ (y = 0–3) (a) $N^+ \rightarrow N^{3+}$, (b) $NH^+ \rightarrow N^{2+}$, (c) $NH_2^+ \rightarrow N^{2+}$, and (d) $NH_3^+ \rightarrow N^{2+}$ measured in the photon energy region of the nitrogen K-edge. The light blue vertical lines mark the energy region of the atomic nitrogen 1s → 2p resonance group in panel (a). For the panels (b)–(d) the shift of the respective molecular resonances to lower excitation energies can be seen. For details of the comparison of the different decay channels of the atomic and molecular targets see the main text.

The curves consist of the N^{3+} ion yield for the atomic N^+ target and the N^{2+} ion yield for the molecular targets NH_y^+ (y = 1–3). The N^{2+} and N^+ product channels, for the N^+ and NH^+ primary beams, respectively, exhibited excessive backgrounds from collisions with residual gas targets such that no meaningful photoinduced ion yields could be measured in these product channels.

The normalised photoinduced ion yield Y is given by the background-subtracted ion count rate R measured with the channeltron detector divided by the target ion current I_{ion} and photon current ϕ_{ph},

$$Y = \frac{R}{I_{ion} \cdot \phi_{ph}}. \quad (2)$$

In principle, the PIPE setup allows one to put the measured ion yields on an absolute cross-section scale.[39] However, for the

Open Access Article. Published on 22 July 2019. Downloaded on 2/20/2026 10:19:23 AM.
This article is licensed under a Creative Commons Attribution 3.0 Unported Licence.

present experiment, there are two unknown quantities: the transmission of the molecular fragments from their point of origin to the detector as well as the exact branching ratio into the measured fragment channel. Still, we can assume that the normalised ion yield Y is proportional to the partial absorption cross section of the respective fragment channel N^{q+}. Upon absorption of an X-ray photon in the energy range of the nitrogen 1s orbital, the ionic targets can either be resonantly excited or, above the threshold, photoionised. In both cases, an inner-shell hole remains which can subsequently decay by an Auger process, thereby changing the charge state of the target. To obtain the observed final fragment charge state $q = 3$ after resonant excitation of N^+ two electrons need to be emitted from the resulting $1s2s^22p^2\,np$ configuration. For configurations where a two-step Auger cascade is energetically not allowed, *i.e.* for $n = 2$, in particular, a double Auger process is required. Such processes are known to appear with a probability of a few percent following atomic K shell ionisation of light elements.[40,53–58] For the molecular ions NH_y^+ (y = 1–3) there are more pathways, resonant and non-resonant, to create the detected N^{2+} fragment compared to the two ionisation processes needed for the N^+ target to reach N^{3+}, since hydrogen partners can leave the system either as neutral atoms or as protons. N^{2+}, for instance, can be created from NH^+ *via* single Auger decay and release of a neutral hydrogen or *via* double Auger decay and release of a proton. From NH_2^+ and NH_3^+ the creation of N^{2+} ions can be expected to be less likely, since it requires more hydrogen to leave the molecule as neutral atoms. This trend is reflected in our data by a steep drop of the N^{2+}-count rate when gradually changing the molecular target from NH^+ to NH_3^+ (with each additional hydrogen the ion yield drops by an order of magnitude). However, since our experimental set-up does not allow us to detect neutral fragments or N^+ ions, we have no measure on competing fragmentation channels.

Distinct characteristic behaviour can be observed in the ion yield spectra of Fig. 2. On the one hand, below the 1s ionisation threshold a strong resonance group is observed in each spectrum which originates in the atomic case from the transition 1s → 2p. At higher energies, except for NH^+, the first 1s ionisation threshold is visible together with Rydberg resonances. Increasing the photon energy and passing the ionisation threshold one may expect an increase in the ion yield, since the initial absorption leads to emission of an electron. For the N^+, NH_2^+, and NH_3^+ cations, such an increase of the ion yield above the threshold is clearly seen. Remarkably, almost no increase in the ion yield is seen for NH^+ (panel b in Fig. 2). This observation may indicate that the mechanisms that lead to creation of N^{2+} ions *via* emission of additional electrons and release of hydrogen atoms differ for the above and below threshold regions for NH^+ and any other ion in the series NH_y^+.

The blue dashed lines in Fig. 2 mark the energy region of the atomic nitrogen 1s → 2p resonance group. As can be seen in the spectra for the molecular ionic series NH_y (y = 1–3), the respective molecular resonance shifts towards lower energies depending on the number of hydrogen atoms bound to the central nitrogen atom. This is due to increasing hybridisation between the nitrogen valence and hydrogen orbitals. For the atomic nitrogen ion N^+, we observe sharp Rydberg lines below and above the lowest 1s ionisation threshold (Fig. 3b), while for the molecular targets the resonance features are broader and overlap with one another. In the following we discuss the assignments of the X-ray absorption resonances for each target NH_y^+ (y = 0–3) in more detail.

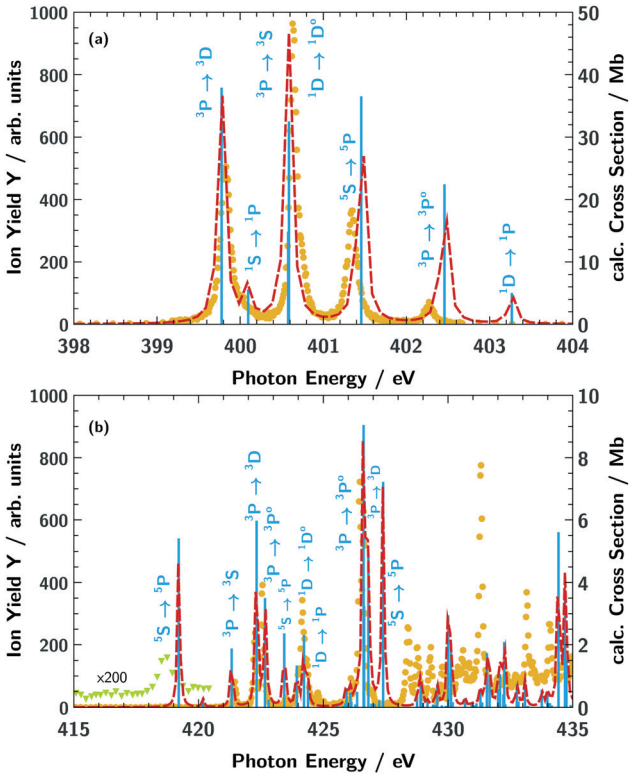

Fig. 3 N^{3+} ion yield Y (orange dots) from photoionisation of the atomic nitrogen target cation N^+ (a) in the energy region of the 1s → 2p excitation and (b) in the energy region of the atomic nitrogen K-edge. The light blue vertical bars indicate the calculated absorption resonance positions and are proportional to the oscillator strength. The red dashed line shows the calculated absorption cross section obtained *via* convolution with a 100 meV (FWHM) Lorentzian function. The light green triangles in panel (b) are a magnification of the ion yield in the respective energy range showing the presence of the 1s → 3p ^{5}P absorption line.

Atomic target N^+

The ground state of the N^+ cation is $1s^22s^22p^2\,{}^3P$. Within the experimental ion beam, a non-statistical mixture of several meta-stable terms exists, as has been pointed out before.[36] These various states result in a multitude of multiplet lines as observed in Fig. 3. For comparison of the measured N^{3+} ion yield (orange dots in Fig. 3) with the calculated X-ray absorption resonance positions (vertical light blue lines in Fig. 3) we take into account the terms $1s^22s^22p^2\,{}^3P$, $1s^22s^22p^2\,{}^1D$, $1s^22s^22p^2\,{}^1S$, and $1s^22s^12p^3\,{}^5S$ with the relative weights of 0.54, 0.11, 0.03, 0.32, respectively, as suggested by Gharaibeh *et al.*[36] For a better comparison, we have shifted the calculated transition energies by 2.1 eV to higher energies for the region showing 1s → 2p excitations (below 405 eV) and by 1.1 eV for the region showing

Open Access Article. Published on 22 July 2019. Downloaded on 2/20/2026 10:19:23 AM.
This article is licensed under a Creative Commons Attribution 3.0 Unported Licence.

higher excitations above 405 eV. Overall, the calculated data show good agreement with the measured ion yield for the energy position of the resonances values below 427 eV. The discrepancies at photon energies above 427 eV are due to the limited capability of the employed basis set to adequatly describe the electronic continuum as discussed in the section Theory Details. For the region below 405 eV, the ion-yield peak heights coincide with the calculated absorption cross section. However, for the region above 415 eV the calculated absorption strength does not always agree with the measured abundance of ions. A particularly drastic disagreement is seen for the $1s^2 2s^1 2p^3\,{}^5S \rightarrow 1s^1 2s^1 2p^3 3p^1\,{}^5P$ transition at 419 eV. The signal in the measured ion yield is remarkably low (magnified by a factor of 200 in Fig. 3b) in contrast to the relatively strong calculated absorption cross section. The $1s^1 2s^1 2p^3 3p^1\,{}^5P$ term, *e.g.*, has a particularly high spin that may lead to blocking of certain Auger decay channels, since the spin of most electrons does not match the spin of the core hole. The production of N^{3+} ions might therefore be suppressed for this core excited configuration relative to other core excited configurations.

Our assignment of the individual resonances for the first resonance region is given in Table 1 and compared with previous calculations using the multi-configuration Dirac–Fock (MCDF) method and the *R*-matrix method.[36] Most of our results match those of previous calculations, however, there is a slight discrepancy regarding the assignment of the $1s^2 2s^1 2p^3\,{}^5S \rightarrow 1s^1 2s^1 2p^4\,{}^5P$ transition. In the previous work[36] this line is, according to the *R*-matrix calculation, associated with the first resonance at 399.8 eV whereas we identify this transitions at $\simeq$401.5 eV (in agreement with the previous MCDF calculation[36]).

Overall we conclude that the applied calculation procedure is sufficient to conduct assignment of the resonant transitions.

Molecular target NH^+

The NH^+ cation has two close lying nearly degenerate terms[31,32] that both result in an absorption signal from our ion beam: $1\sigma^2 2\sigma^2 3\sigma^2 1\pi^1\,{}^2\Pi$ and $1\sigma^2 2\sigma^2 3\sigma^1 1\pi^2\,{}^4\Sigma^-$.

With our geometry optimisation we obtained a bond distance of 1.065 Å for the $^2\Pi$ term and of 1.080 Å for the $^4\Sigma^-$ term. Fig. 4 shows the calculated absorption resonances (light blue vertical lines) for the NH^+ cation compared to the measured N^{2+} ion yield (dark blue dots). In the figure we used 0.8 and 0.2 as weights for the $^2\Pi$ and $^4\Sigma^-$ terms, respectively. The red dashed line in Fig. 4 is the result of a convolution of the calculated resonances characterised by their positions and absorption oscillator strengths with a 400 meV FWHM Gaussian function for the lower energy part (392 eV to 404 eV) and with 3 eV FWHM Gaussian function for the higher energy part. As for the spectrum of the atomic N^+ ion, the calculated transition lines have been shifted by 2.1 eV for the region 390 eV to 405 eV and by 1.1 eV for the region above 405 eV.

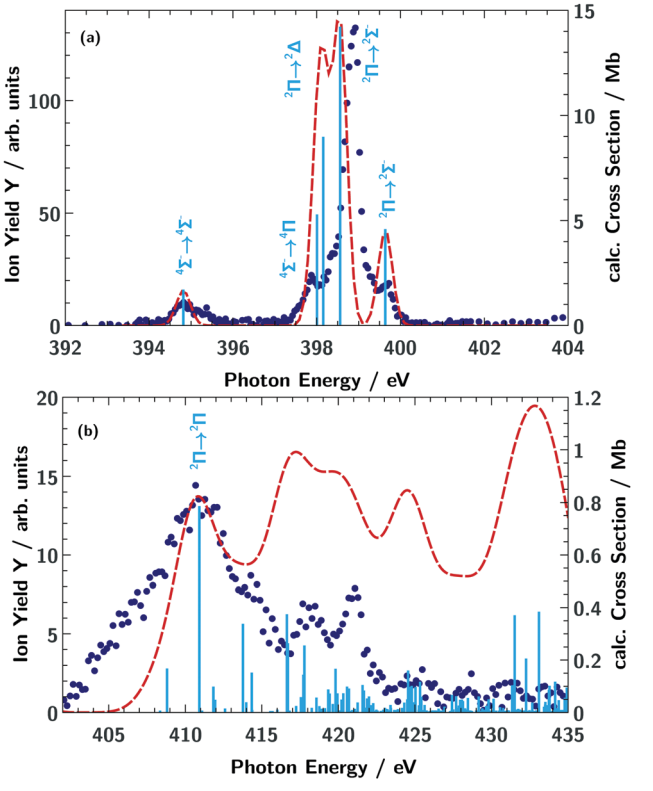

Fig. 4 N^{2+} ion yield *Y* (dark blue dots) for the NH^+ cation (a) in the energy region of the 1s → 2p excitation of atomic nitrogen and (b) in the energy region of the atomic nitrogen K-edge. The light blue vertical bars indicate the calculated absorption resonance positions and are proportional to the oscillator strength. The red dashed line shows the calculated absorption cross section obtained *via* convolution with a 400 meV (panel a) (FWHM) and 3 eV (panel b) (FWHM) Gaussian function.

In the region below 405 eV one can clearly identify four peaks in the experimental spectrum. The weak resonance at 395 eV can be assigned to a $1\sigma^4\Sigma^- \rightarrow 3\sigma^4\Sigma^-$ excitation. In the region 397 eV to 400 eV our calculation predicts four excitation resonances $^4\Sigma^- \rightarrow {}^4\Pi$, $^2\Pi \rightarrow {}^2\Delta$, $^2\Pi \rightarrow {}^2\Sigma^-$, and $^2\Pi \rightarrow {}^2\Sigma^+$. However, in the measured ion yield one can clearly resolve three peaks, only. The calculation suggests that the $^2\Pi \rightarrow {}^2\Delta$ transition is hidden between the $^4\Sigma \rightarrow {}^4\Pi$ and the $^2\Pi \rightarrow {}^4\Sigma^-$ resonances. The remaining resonance peak at 399.5 eV can be associated with a $^2\Pi \rightarrow {}^2\Sigma^-$ transition.

Above an excitation energy of 405 eV the resonance structures in the measured ion yield are very broad. This might be attributed to the large broadening due to a steep potential energy curve in the final state. The resonance at 411 eV is rather isolated. According to our calculation, the dominant broad peak around 411 eV can mainly be assigned to a $1\sigma \rightarrow 4\sigma$ ($^2\Pi \rightarrow {}^2\Pi$) excitation. Above 415 eV we see the ion yield

Table 1 Comparison of calculated resonance positions E_{ph} for N^+

Resonance transition	CI present work (eV)	MCDF (eV) Gharaibeh *et al.*[36]	*R*-Matrix (eV)
$1s^2 2s^2 2p^2\,{}^3P \rightarrow 1s^1 2s^2 2p^3\,{}^3D$	399.8	399.9	399.7
$1s^2 2s^2 2p^2\,{}^1S \rightarrow 1s^1 2s^2 2p^3\,{}^1P$	400.1	400.6	400.2
$1s^2 2s^2 2p^2\,{}^3P \rightarrow 1s^1 2s^2 2p^3\,{}^3S$	400.6	400.0	400.6
$1s^2 2s^2 2p^2\,{}^1D \rightarrow 1s^1 2s^2 2p^3\,{}^1D$	400.6	400.0	400.7
$1s^2 2s^1 2p^3\,{}^5S \rightarrow 1s^1 2s^1 2p^4\,{}^5P$	401.5	400.8	399.9
$1s^2 2s^2 2p^2\,{}^3P \rightarrow 1s^1 2s^2 2p^3\,{}^3P$	402.5	402.3	401.3
$1s^2 2s^2 2p^2\,{}^1D \rightarrow 1s^1 2s^2 2p^3\,{}^1P$	403.3	402.5	402.3

Open Access Article. Published on 22 July 2019. Downloaded on 2/20/2026 10:19:23 AM.
This article is licensed under a Creative Commons Attribution 3.0 Unported Licence.

Table 2 Resonance positions E_{ph} and line assignment of the observed resonances in the NH^+ molecular target ion (see Fig. 4). The assignment is done according to the dominant CI configuration. The uncertainty of the experimental values is ΔE_{ph} = 0.1 eV

Resonance assignment			
Initial state		PIPE (experiment) (eV)	CI (theory) (eV)
$1\sigma^2 2\sigma^2 3\sigma^1 1\pi^2\ ^4\Sigma^-$	$1\sigma \rightarrow 3\sigma^4\Sigma^-$	394.9	394.8
	$1\sigma \rightarrow 1\pi^4\Pi$	397.8	398.0
	$1\sigma \rightarrow 4\sigma^4\Sigma^-$		409.3
	$1\sigma \rightarrow 4\sigma^4\Sigma^-$		412.4
$1\sigma^2 2\sigma^2 3\sigma^2 1\pi^1\ ^2\Pi$	$1\sigma \rightarrow 1\pi^2\Delta$	398.8	398.2
	$1\sigma \rightarrow 1\pi^2\Sigma^-$	398.8	398.6
	$1\sigma \rightarrow 1\pi^2\Sigma^+$	399.6	399.7
	$1\sigma \rightarrow 4\sigma^4\Pi$		411.4
	$1\sigma \rightarrow 4\sigma^4\Pi$		414.3

decreasing with photon energy, whereas the calculated convoluted absorption cross section suggests rather the opposite trend. The assignments for the dominant transitions in the NH^+-XAS are summarised in Table 2.

Molecular target NH_2^+

The NH_2^+ molecular cation has C_{2v} symmetry, but has an almost linear geometry with a very flat bending potential in its ground state.[59,60] The cationic ground level is $(1a_1)^2(2a_1)^2(1b_2)^2(3a_1)^1(1b_1)^1\ ^3B_1$. For the X-ray absorption calculation we also included the closed shell level $(1a_1)^2(2a_1)^2(1b_2)^2(3a_1)^2\ ^1A_1$.

From geometry optimisation, we obtain an NH bond distance of 1.03 Å and a bond angle of 150° for the triplet level and a bond distance of 1.05 Å with a bond angle of 107° for the singlet level. Fig. 5 shows the calculated absorption resonance positions (light blue vertical lines) for the NH_2^+ cation compared to the measured N^{2+} ion yield (green dots). The orange dashed line is a convolution of the calculated resonance position and strength with a 1.0 eV FWHM Gaussian function. For better comparison, the calculated absorption lines have been shifted by 1.8 eV in the region below 405 eV and by 1.0 eV in the region above 405 eV. Because of the almost linear geometry of the molecular cation, the $1a_1 \rightarrow 3a_1\ ^3B_1$ and $1a_1 \rightarrow 1b_1\ ^3A_1$ excitations are almost degenerate. As can be seen in Fig. 5a, the calculated positions of these two resonances agree with the ion yield peak at 396 eV. The $1a_1 \rightarrow 1b_1$ resonance for the tilted geometry of the $^1A_1$ cationic level is at distinguishably higher energies.

For the higher excitation energies above 405 eV, the observed ion yield peaks can be assigned to calculated absorption lines of the $3B_1$ initial level into dipole-allowed higher excited levels of the irreducible representations $^3B_1$ or $^3A_2$. Overall good agreement can be seen for resonances up to 420 eV. The assignments are summarised in Table 3.

Molecular target NH_3^+

The neutral NH_3 molecule has a pyramidal geometry and hence its symmetry group is C_{3v}.[25,27] The cation NH_3^+ has a planar geometry and thus belongs to symmetry group D_{3h}.[61] The electronic

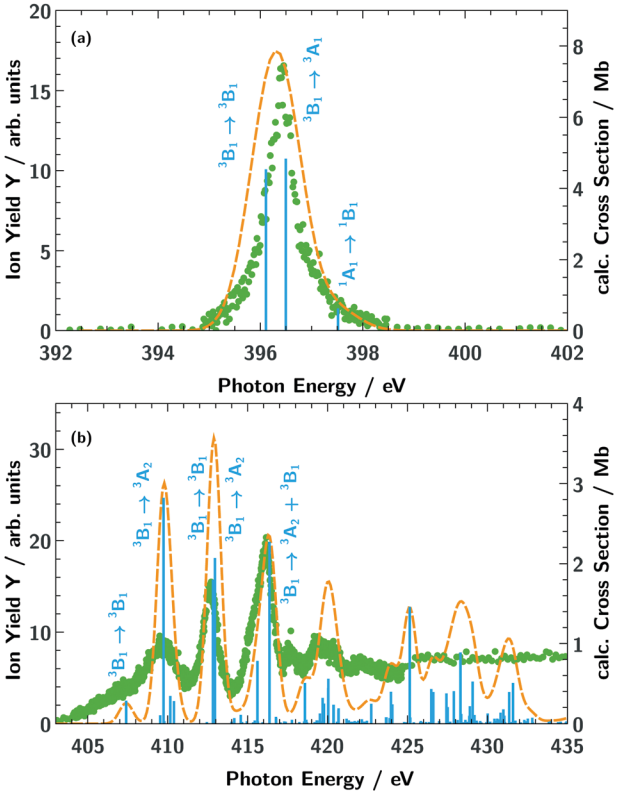

Fig. 5 N^{2+} ion yield Y (green dots) from the photo-fragmentation of the NH_2^+ cation (a) in the energy region of the 1s → 2p excitation of atomic nitrogen and (b) in the energy region of the atomic nitrogen K-edge. The light blue vertical bars indicate the calculated absorption resonance positions and are proportional to the oscillator strength. The orange dashed line shows the calculated absorption cross section obtained *via* convolution with a 1.0 eV (FWHM) Gaussian function.

ground state of the cation is $\left(1a_1'\right)^2\left(2a_1'\right)^2\left(1e'\right)^4\left(1a_2''\right)^1\ ^2A_2''$. Geometry optimisation gives an NH bond length of 1.024 Å. Fig. 6 compares the calculated absorption lines (light blue vertical lines) for the NH_3^+ cation with the measured N^{2+} ion yield (red dots). The orange dashed line is a convolution of the calculated resonance position and strength with a 1.0 eV FWHM Gaussian function. The calculated transitions have been shifted by 1.6 eV for the region below 405 eV and by 1.2 eV above 405 eV.

Below 405 eV the single ion yield peak must be associated with the $1a_1' \rightarrow 1a_2''\ ^2A_1'$ excitation, as indicated by the calculated transition. Above 405 eV several peaks can be observed in the measured ion yield. These peaks match with those of the calculated transitions into higher excited states up to excitation energies of 420 eV. The assignment of individual resonances is summarised in Table 4.

Chemical shift

As indicated by the light blue dashed lines in Fig. 2, the respective 1s → 2p resonances shift to lower excitation energies when going from the atomic cation N^+ to the molecular cation NH_3^+. For the energies of the 1s → 2p resonance peaks, we obtain a systematic sequence of 399.8 eV, 398.8 eV, 396.4 eV,

 This journal is © the Owner Societies 2019

Open Access Article. Published on 22 July 2019. Downloaded on 2/20/2026 10:19:23 AM.
This article is licensed under a Creative Commons Attribution 3.0 Unported Licence.

Table 3 Resonance positions E_{ph} in and line assignments of the observed resonances in the NH_2^+ molecular target ion (see Fig. 5) in its cationic ground level ($(1a_1)^2(2a_1)^2(1b_2)^2(3a_1)^1(1b_1)^1\,^3B_1$) or excited level ($(1a_1)^2(2a_1)^2(1b_2)^2(3a_1)^2\,^1A_1$). The assignment is done according to the dominant CI configuration. The uncertainty of the experimental values is ΔE_{ph} = 0.1 eV

Resonance assignment			
Initial state (val. conf.)		PIPE (experiment) (eV)	CI (theory) (eV)
$(3a_1)^1(1b_1)^1\,^3B_1$	$1a_1 \rightarrow 3a_1\,^3B_1$	396.4	396.1
	$1a_1 \rightarrow 1b_1\,^3A_1$	396.4	396.5
	$1a_1 \rightarrow 4a_1\,^3B_1$	407.2	407.4
	$1a_1 \rightarrow 2b_2\,^3A_2$	409.6	409.8
	$1a_1 \rightarrow 2b_1\,^3A_1$	412.7	412.8
	$1a_1 \rightarrow 5a_1\,^3B_1$	412.7	412.8
	$1a_1 \rightarrow 2b_2\,^3A_2$		413.0
	$1a_1 \rightarrow 3b_2\,^3A_2$	416.1	415.6
	$1a_1 \rightarrow 2b_1\,^3A_1$	416.1	416.4
	$1a_1 \rightarrow 5a_1\,^3B_1$	416.1	416.4
$(3a_1)^2\,^1A_1$	$1a_1 \rightarrow 1b_1\,^1B_1$		397.5
	$1a_1 \rightarrow 4a_1\,^1A_1$		410.2
	$1a_1 \rightarrow 2b_2\,^1B_2$		411.4
	$1a_1 \rightarrow 2b_1\,^1B_1$		415.4
	$1a_1 \rightarrow 5a_1\,^1A_1$		415.6

395.2 eV. With more hydrogen atoms in the molecule, additional electrons contribute to core-hole screening effects[62] and lower the energy of the core excited state. As discussed previously,[42] this effect leads to a systematic lowering of core excitation resonances. To further confirm this trend, we calculated the ionisation potential of the molecular cations using a Δ SCF calculation, in which the ionisation energy is obtained from separate SCF calculations for the initial and final electronic states, respectively (see Table 5). As can be seen, apart from the metastable configurations that involve vacancies in 2s/3σ orbitals (^5S for N^+ and $^4\Sigma^+$ for NH^+), the ionisation potential shifts systematically to lower energies with increasing number of hydrogen atoms.

At 400 eV, in Fig. 2 a clear shift of the resonant structures to lower photon energies with increasing number y of H atoms is found for the series of free NH_y^+ ions. This is contrary to shifts found for the alkylamines,[37] where the N 1s resonances are shifting to higher photon energy with increasing number of H atoms.

Absolute count rate for the lower and upper resonance regions

As indicated by the different scale on the calculated cross section axes in Fig. 3–6(a) and (b), the absorption lines for the higher Rydberg region (>415 eV) are weaker than for the first resonance region (390 eV to 405 eV). In contrast, the measured N^{2+} ion yield is significantly larger in the Rydberg region compared to the first resonance region. This clearly indicates that the relative probability for creating N^{2+} ions is larger for the more highly excited resonances than for the resonances with lower excitation energies. The relative production yields of N^{2+} subsequent to excitation into these two resonance regions can be read off the relative change of the ion yield/cross section scale in Fig. 3–6. For N^+ we observe a factor ≃5 higher N^{2+} production rate, for NH^+ the factor is ≃1.8, for NH_2^+ the factor is ≃3.7, and for NH_3^+ the factor is ≃2.3.

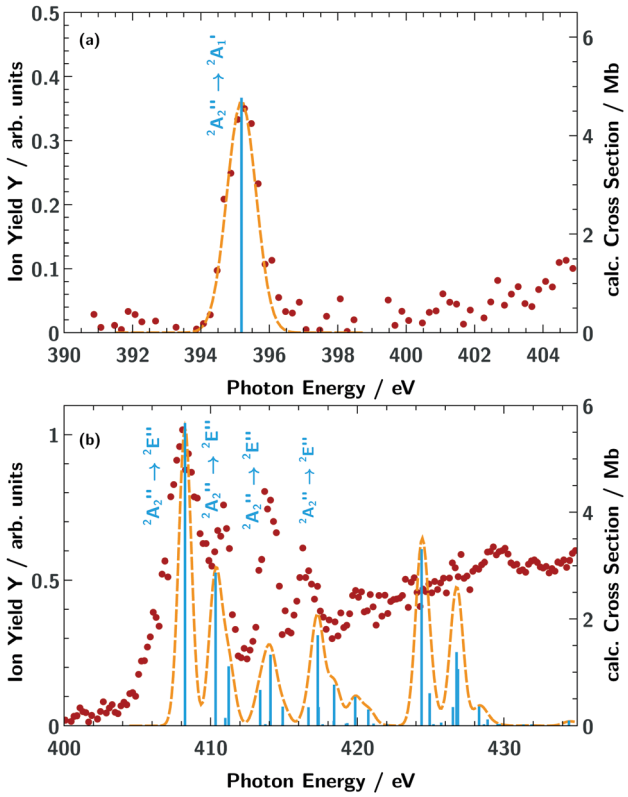

Fig. 6 N^{2+} ion yield Y (red dots) from the photo-fragmentation of the NH_3^+ cation (a) in the energy region of the 1s → 2p excitation of atomic nitrogen and (b) in the energy region of the atomic nitrogen K-edge. The light blue vertical bars are proportional to the calculated oscillator strength and indicate the absorption resonance position. The orange dashed line shows the calculated absorption cross section obtained *via* convolution with a 1.0 eV (FWHM) Gaussian function.

Comparison with glycine

Fig. 7 shows a comparison between the absorption spectrum of glycine around the nitrogen K-edge[63] and our measured ion yield of NH_2^+. The data of glycine was scaled to match the intensity at energies above the K-edge and the figure is drawn with two different energy axes, because of the different chemical environment of the two molecules. As can be seen, the first

Table 4 Resonance positions E_{ph} and line assignments of the observed resonances in the NH_3^+ molecular target ion in its ground level ($(1a_1')^2(2a_1')^2(1e')^4(1a_2'')^1\,^2A_2''$) (see Fig. 6). The assignment is done according to the dominant CI configuration. The uncertainty of the experimental values is ΔE_{ph} = 0.1 eV

Resonance		
Assignment	PIPE (experiment) (eV)	CI (theory) (eV)
$1a_1' \rightarrow 1a'' {}^2A_1'$	395.2	395.2
$1a_1' \rightarrow 2e' {}^2E''$	408.1	408.3
$1a_1' \rightarrow 2e' {}^2E''$	410.8	410.3
$1a_1' \rightarrow 2a_2'' {}^2A_1'$	410.8	411.2
$1a_1' \rightarrow 2a_2'' {}^2A_1'$	413.9	413.4
$1a_1' \rightarrow 3e'1 {}^2E''$	413.9	414.1
$1a_1' \rightarrow 4e' {}^2E''$	413.9	417.3

Open Access Article. Published on 22 July 2019. Downloaded on 2/20/2026 10:19:23 AM.
This article is licensed under a Creative Commons Attribution 3.0 Unported Licence.

Table 5 Ionisation potentials for the series NH_y^+ (y = 0–3) obtained by a Δ SCF calculation

Ion	Limit term	Δ SCF ionisation potential (eV)
N^+	^4P	431.3
N^+	^2D	433.7
N^+	^2S	434.7
N^+	^6S	426.4
NH^+	$^3\Pi$	427.3
NH^+	$^5\Sigma^-$	422.5
NH_2^+	$^4B_1$	420.3
NH_2^+	$^2A_1$	423.3
NH_3^+	$^3A_2''$	418.5

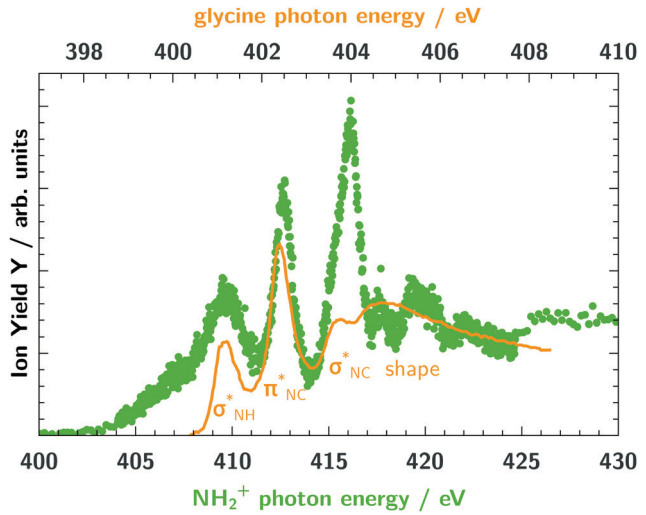

Fig. 7 Comparison of the ion yield of the molecular ion NH_2^+ (green dots) and the absorption spectrum of glycine[63] (orange line) at the nitrogen K-edge. The photon energy and ion yield scale of glycine is shifted and scaled to match NH_2^+. The two photon energy axes have different step widths.

resonances below the K-edge are prominent in both spectra, but at higher energies the resonances are much smoother in glycine. The three resonances for glycine are assigned to excitations into virtual orbitals with the local $\sigma^*_{NH}, \pi^*_{NC}, \sigma^*_{NC}$ orbital character.[63] This assignment matches the assignment for NH_2^+ attributing the three major resonances mainly to excitations into the $2b_2$, $2b_1$, and $5a_1$ orbitals, corresponding to local σ^*_{NH}, p_x, and p_y orbital character, respectively.

In contrast, the spectra of glycine shows some significant differences compared to the spectra of NH_3^+ (see Fig. 6). Thus, this comparison between NH_2^+, NH_3^+ and glycine demonstrates that the spectra of ionic fragments can be useful to identify building blocks of more complex molecules.

Conclusions

The N^{2+} ion yields of the target molecular cations NH_y^+ (y = 1–3) have been measured in the energy range of the nitrogen K-edge and their absorption resonance structure has been determined. We have calculated X-ray absorption cross sections based on the configuration interaction method utilising the XMOLECULE toolkit. Our calculations show excellent agreement with the ion yield data. For most of the observed transitions, the ion yield seems to correlate with the calculated absorption strength. However, we quantify a trend for a lower abundance of N^{2+} ions for excitation in the first resonance region compared to higher resonances. This trend as well as particular deviations (*e.g.*, the very low ion yield for the N^+ $1s^2 2s^1 2p^3\ ^5S \rightarrow 1s^1 2s^1 2p^3 3p^1\ ^5P$ transition) indicate that the mechanism behind the production of the highly charged ions depends on the specific state populated by the X-ray absorption. In future studies, this effect will be further investigated by comparing the relative ion yields of different fragment charges.

The measured ion yield resonances have been identified by the calculated absorption transitions (see Tables 2–4). Depending on the number of hydrogen atoms bound to the nitrogen atom we report characteristic structures in the X-ray absorption. Each additional hydrogen atom and its electron has a significant impact on the spectral features of the different absorption spectra (Fig. 2). These characteristic resonance structures in the NH_y^+ series might help to identify different molecular cationic (sub-)groups within larger molecular complexes such as the amino acid glycine, for example. Nevertheless, the comparison of the free ions NH_y^+ with the amine group in different solutions and molecular environments shows the tremendous influence also of the larger chemical surrounding.

Conflicts of interest

There are no conflicts to declare.

Acknowledgements

This research was carried out at the synchrotron light source PETRA III at DESY, a member of the Helmholtz Association (HGF). We would like to thank J. Buck, G. Hartmann, F. Scholz, J. Seltmann, and J. Viefhaus for assistance in using beamline P04. The design and construction of PIPE and this work was funded by German ministry for education and research (BMBF) under contracts 05KS7RG1, 05KS7GU2, 05KS7KE1, 05KS7RF2, 05K10RG1, 05K10GUB, 05K10KEA, and 05K10RF2 within the "Verbundforschung" funding scheme. KM and MM acknowledge funding by the Deutsche Forschungsgemeinschaft (DFG) *via* SFB925/A3. AM acknowledges funding by Deutsche Forschungsgemeinschaft *via* grant Mu 1068/22. SK acknowledges the funding of the EUCALL project within the European Union's Horizon 2020 research and innovation programme under the grant agreement no. 654220. SDö, SDe, LS, KS, and SB were supported by the Helmholtz Initiative and Networking Fund through the Young Investigator Groups Program. KS and SB acknowledge support from the Deutsche Forschungsgemeinschaft, project B03/SFB755.

Open Access Article. Published on 22 July 2019. Downloaded on 2/20/2026 10:19:23 AM.
This article is licensed under a Creative Commons Attribution 3.0 Unported Licence.

Notes and references

1 H. N. Chapman, P. Fromme, A. Barty, T. A. White, R. A. Kirian, A. Aquila, M. S. Hunter, J. Schulz, D. P. DePonte, U. Weierstall, R. B. Doak, F. R. N. C. Maia, A. V. Martin, I. Schlichting, L. Lomb, N. Coppola, R. L. Shoeman, S. W. Epp, R. Hartmann, D. Rolles, A. Rudenko, L. Foucar, N. Kimmel, G. Weidenspointner, P. Holl, M. Liang, M. Barthelmess, C. Caleman, S. Boutet, M. J. Bogan, J. Krzywinski, C. Bostedt, S. Bajt, L. Gumprecht, B. Rudek, B. Erk, C. Schmidt, A. Homke, C. Reich, D. Pietschner, L. Struder, G. Hauser, H. Gorke, J. Ullrich, S. Herrmann, G. Schaller, F. Schopper, H. Soltau, K.-U. Kuhnel, M. Messerschmidt, J. D. Bozek, S. P. Hau-Riege, M. Frank, C. Y. Hampton, R. G. Sierra, D. Starodub, G. J. Williams, J. Hajdu, N. Timneanu, M. M. Seibert, J. Andreasson, A. Rocker, O. Jonsson, M. Svenda, S. Stern, K. Nass, R. Andritschke, C.-D. Schroter, F. Krasniqi, M. Bott, K. E. Schmidt, X. Wang, I. Grotjohann, J. M. Holton, T. R. M. Barends, R. Neutze, S. Marchesini, R. Fromme, S. Schorb, D. Rupp, M. Adolph, T. Gorkhover, I. Andersson, H. Hirsemann, G. Potdevin, H. Graafsma, B. Nilsson and J. C. H. Spence, *Nature*, 2011, **470**, 73.

2 H. N. Chapman, C. Caleman and N. Timneanu, *Philos. Trans. R. Soc., B*, 2014, **369**, 20130313.

3 J. Czapla-Masztafiak, J. Szlachetko, C. Milne, E. Lipiec, J. Sá, T. Penfold, T. Huthwelker, C. Borca, R. Abela and W. Kwiatek, *Biophys. J.*, 2016, **110**, 1304.

4 S. Bari, D. Egorov, T. L. C. Jansen, R. Boll, R. Hoekstra, S. Techert, V. Zamudio-Bayer, C. Bülow, R. Lindblad, G. Leistner, A. Ławicki, K. Hirsch, P. S. Miedema, B. von Issendorff, J. T. Lau and T. Schlathölter, *Chem. – Eur. J.*, 2018, **24**, 7631.

5 A. Barty, J. Küpper and H. N. Chapman, *Annu. Rev. Phys. Chem.*, 2013, **64**, 415.

6 C. Kupitz, S. Basu, I. Grotjohann, R. Fromme, N. A. Zatsepin, K. N. Rendek, M. S. Hunter, R. L. Shoeman, T. A. White, D. Wang, D. James, J.-H. Yang, D. E. Cobb, B. Reeder, R. G. Sierra, H. Liu, A. Barty, A. L. Aquila, D. Deponte, R. A. Kirian, S. Bari, J. J. Bergkamp, K. R. Beyerlein, M. J. Bogan, C. Caleman, T.-C. Chao, C. E. Conrad, K. M. Davis, H. Fleckenstein, L. Galli, S. P. Hau-Riege, S. Kassemeyer, H. Laksmono, M. Liang, L. Lomb, S. Marchesini, A. V. Martin, M. Messerschmidt, D. Milathianaki, K. Nass, A. Ros, S. Roy-Chowdhury, K. Schmidt, M. Seibert, J. Steinbrener, F. Stellato, L. Yan, C. Yoon, T. A. Moore, A. L. Moore, Y. Pushkar, G. J. Williams, S. Boutet, R. B. Doak, U. Weierstall, M. Frank, H. N. Chapman, J. C. H. Spence and P. Fromme, *Nature*, 2014, **513**, 261.

7 I. D. Young, M. Ibrahim, R. Chatterjee, S. Gul, F. D. Fuller, S. Koroidov, A. S. Brewster, R. Tran, R. Alonso-Mori, T. Kroll, T. Michels-Clark, H. Laksmono, R. G. Sierra, C. A. Stan, R. Hussein, M. Zhang, L. Douthit, M. Kubin, C. de Lichtenberg, L. Vo Pham, H. Nilsson, M. H. Cheah, D. Shevela, C. Saracini, M. A. Bean, I. Seuffert, D. Sokaras, T.-C. Weng, E. Pastor, C. Weninger, T. Fransson, L. Lassalle, P. Bräuer, P. Aller, P. T. Docker, B. Andi, A. M. Orville, J. M. Glownia, S. Nelson, M. Sikorski, D. Zhu, M. S. Hunter, T. J. Lane, A. Aquila, J. E. Koglin, J. Robinson, M. Liang, S. Boutet, A. Y. Lyubimov, M. Uervirojnangkoorn, N. W. Moriarty, D. Liebschner, P. V. Afonine, D. G. Waterman, G. Evans, P. Wernet, H. Dobbek, W. I. Weis, A. T. Brunger, P. H. Zwart, P. D. Adams, A. Zouni, J. Messinger, U. Bergmann, N. K. Sauter, J. Kern, V. K. Yachandra and J. Yano, *Nature*, 2016, **540**, 453.

8 T. J. Penfold, I. Tavernelli, C. J. Milne, M. Reinhard, A. E. Nahhas, R. Abela, U. Rothlisberger and M. Chergui, *J. Chem. Phys.*, 2013, **138**, 014104.

9 R. Kaschner and D. Hohl, *J. Phys. Chem. A*, 1998, **102**, 5111.

10 N. Mardirossian and M. Head-Gordon, *Mol. Phys.*, 2017, **115**, 2315.

11 T. Andersen, H. Kjeldsen, H. Knudsen and F. Folkmann, *J. Phys. B: At., Mol. Opt. Phys.*, 2001, **34**, L327.

12 G. Hinojosa, A. M. Covington, R. A. Phaneuf, M. M. Sant'Anna, R. Hernandez, I. R. Covington, I. Domínguez, J. D. Bozek, A. S. Schlachter, I. Álvarez and C. Cisneros, *Phys. Rev. A: At., Mol., Opt. Phys.*, 2002, **66**, 032718.

13 G. Hinojosa, M. M. Sant'Anna, A. M. Covington, R. A. Phaneuf, I. R. Covington, I. Domínguez, A. S. Schlachter, I. Alvarez and C. Cisneros, *J. Phys. B: At., Mol. Opt. Phys.*, 2005, **38**, 2701.

14 J.-P. Mosnier, E. T. Kennedy, P. van Kampen, D. Cubaynes, S. Guilbaud, N. Sisourat, A. Puglisi, S. Carniato and J.-M. Bizau, *Phys. Rev. A*, 2016, **93**, 061401.

15 A. Puglisi, T. Miteva, E. T. Kennedy, J.-P. Mosnier, J.-M. Bizau, D. Cubaynes, N. Sisourat and S. Carniato, *Phys. Chem. Chem. Phys.*, 2018, **20**, 4415.

16 C. Nordling, E. Sokolowski and K. Siegbahn, *Phys. Rev.*, 1957, **105**, 1676.

17 O. Travnikova, K. J. Børve, M. Patanen, J. Söderström, C. Miron, L. J. Sæthre, N. Mårtensson and S. Svensson, *J. Electron Spectrosc. Relat. Phenom.*, 2012, **185**, 191.

18 N. Mårtensson, E. Sokolowski and S. Svensson, *J. Electron Spectrosc. Relat. Phenom.*, 2014, **193**, 27.

19 J. Higuchi, *J. Chem. Phys.*, 1956, **24**, 535.

20 G. Wight and C. Brion, *J. Electron Spectrosc. Relat. Phenom.*, 1974, **4**, 25.

21 R. N. Sodhi and C. Brion, *J. Electron Spectrosc. Relat. Phenom.*, 1985, **36**, 187.

22 S. Y. T. van de Meerakker, I. Labazan, S. Hoekstra, J. Küpper and G. Meijer, *J. Phys. B: At., Mol. Opt. Phys.*, 2006, **39**, S1077.

23 B.-M. Cheng, H.-C. Lu, H.-K. Chen, M. Bahou, Y.-P. Lee, A. M. Mebel, L. C. Lee, M.-C. Liang and Y. L. Yung, *ApJ*, 2006, **647**, 1535.

24 D. Edvardsson, P. Baltzer, L. Karlsson, B. Wannberg, D. M. P. Holland, D. A. Shaw and E. E. Rennie, *J. Phys. B: At., Mol. Opt. Phys.*, 1999, **32**, 2583.

25 J. Schirmer, A. B. Trofimov, K. J. Randall, J. Feldhaus, A. M. Bradshaw, Y. Ma, C. T. Chen and F. Sette, *Phys. Rev. A: At., Mol., Opt. Phys.*, 1993, **47**, 1136.

26 A. Jürgensen and R. G. Cavell, *Chem. Phys.*, 2001, **273**, 77.

Open Access Article. Published on 22 July 2019. Downloaded on 2/20/2026 10:19:23 AM.
This article is licensed under a Creative Commons Attribution 3.0 Unported Licence.

27 K. Jakubowska, G. Vall-llosera, A. Kivimäki, M. Coreno, E. M. García, M. Stankiewicz and E. Rachlew, *J. Phys. B: At., Mol. Opt. Phys.*, 2007, **40**, 1489.
28 N. Walsh, A. Sankari, J. Laksman, T. Andersson, S. Oghbaie, F. Afaneh, E. P. Mansson, M. Gisselbrecht and S. L. Sorensen, *Phys. Chem. Chem. Phys.*, 2015, **17**, 18944.
29 Y.-J. Wu, H.-C. Lu, H.-K. Chen, B.-M. Cheng, Y.-P. Lee and L. C. Lee, *J. Chem. Phys.*, 2007, **127**, 154311.
30 Y. Senba, T. Goya, H. Yoshida and A. Hiraya, *J. Electron Spectrosc. Relat. Phenom.*, 2005, **144**, 195.
31 J. M. Amero and G. J. Vázquez, *Int. J. Quantum Chem.*, 2004, **99**, 353.
32 J. M. Amero and G. J. Vázquez, *Int. J. Quantum Chem.*, 2005, **101**, 396.
33 J. C. Stephens, Y. Yamaguchi and H. F. Schaefer III, *THEOCHEM*, 1999, **461**, 41.
34 S. Willitsch, F. Merkt, M. Kállay and J. Gauss, *Mol. Phys.*, 2006, **104**, 1457.
35 J. Lecointre, J. J. Jureta and P. Defrance, *J. Phys. B: At., Mol. Opt. Phys.*, 2010, **43**, 105202.
36 M. F. Gharaibeh, J. M. Bizau, D. Cubaynes, S. Guilbaud, N. El Hassan, M. M. Al Shorman, C. Miron, C. Nicolas, E. Robert, C. Blancard and B. M. McLaughlin, *J. Phys. B: At., Mol. Opt. Phys.*, 2011, **44**, 175208.
37 M. Ekimova, M. Kubin, M. Ochmann, J. Ludwig, N. Huse, P. Wernet, M. Odelius and E. T. J. Nibbering, *J. Phys. Chem. B*, 2018, **122**, 7737.
38 M. Ekimova, W. Quevedo, Ł. Szyc, M. Iannuzzi, P. Wernet, M. Odelius and E. T. J. Nibbering, *J. Am. Chem. Soc.*, 2017, **139**, 12773.
39 S. Schippers, S. Ricz, T. Buhr, A. B. Jr, J. Hellhund, K. Holste, K. Huber, H.-J. Schäfer, D. Schury, S. Klumpp, K. Mertens, M. Martins, R. Flesch, G. Ulrich, E. Rühl, T. Jahnke, J. Lower, D. Metz, L. P. H. Schmidt, M. Schöffler, J. B. Williams, L. Glaser, F. Scholz, J. Seltmann, J. Viefhaus, A. Dorn, A. Wolf, J. Ullrich and A. Müller, *J. Phys. B: At., Mol. Opt. Phys.*, 2014, **47**, 115602.
40 A. Müller, D. Bernhardt, A. Borovik Jr., T. Buhr, J. Hellhund, K. Holste, A. Kilcoyne, S. Klumpp, M. Martins, S. Ricz, J. Seltmann, J. Viefhaus and S. Schippers, *ApJ*, 2017, **836**, 166.
41 J. Viefhaus, F. Scholz, S. Deinert, L. Glaser, M. Ilchen, J. Seltmann, P. Walter and F. Siewert, *Nucl. Instrum. Methods Phys. Res., Sect. A*, 2013, **710**, 151.
42 S. Klumpp, A. A. Guda, K. Schubert, K. Mertens, J. Hellhund, A. Müller, S. Schippers, S. Bari and M. Martins, *Phys. Rev. A*, 2018, **97**, 033401.
43 R. Trassl, P. Hathiramani, F. Broetz, J. B. Greenwood, R. W. McCullough, M. Schlapp and E. Salzborn, *Phys. Scr.*, 1997, **1997**, 380.
44 M. Berglund and M. Wieser, *Pure Appl. Chem.*, 2011, **83**, 397.
45 Y. Hao, L. Inhester, K. Hanasaki, S.-K. Son and R. Santra, *Struct. Dyn.*, 2015, **2**, 041707.
46 L. Inhester, K. Hanasaki, Y. Hao, S.-K. Son and R. Santra, *Phys. Rev. A*, 2016, **94**, 023422.
47 M. W. Schmidt, K. K. Baldridge, J. A. Boatz, S. T. Elbert, M. S. Gordon, J. H. Jensen, S. Koseki, N. Matsunaga, K. A. Nguyen, S. Su, T. L. Windus, M. Dupuis and J. A. Montgomery, *J. Comput. Chem.*, 1993, **14**, 1347.
48 R. Krishnan, J. S. Binkley, R. Seeger and J. A. Pople, *J. Chem. Phys.*, 1980, **72**, 650.
49 K. Kaufmann, W. Baumeister and M. Jungen, *J. Phys. B: At., Mol. Opt. Phys.*, 1989, **22**, 2223.
50 Q. Sun, *J. Comput. Chem.*, 2015, **36**, 1664.
51 R. Arneberg, H. Ågren, J. Müller and R. Manne, *Chem. Phys. Lett.*, 1982, **91**, 362.
52 H. Ågren and R. Arneberg, *Phys. Scr.*, 1983, **28**, 80.
53 T. A. Carlson and M. O. Krause, *Phys. Rev. Lett.*, 1965, **14**, 390–392.
54 T. A. Carlson and M. O. Krause, *Phys. Rev. Lett.*, 1966, **17**, 1079–1083.
55 N. Saito and I. H. Suzuki, *Phys. Scr.*, 1994, **49**, 80.
56 B. Kanngießer, M. Jainz, S. Brünken, W. Benten, C. Gerth, K. Godehusen, K. Tiedtke, P. van Kampen, A. Tutay, P. Zimmermann, V. F. Demekhin and A. G. Kochur, *Phys. Rev. A: At., Mol., Opt. Phys.*, 2000, **62**, 014702.
57 A. Müller, A. Borovik, T. Buhr, J. Hellhund, K. Holste, A. Kilcoyne, S. Klumpp, M. Martins, S. Ricz, J. Viefhaus and S. Schippers, *Phys. Rev. Lett.*, 2015, **114**, 013002.
58 S. Schippers, R. Beerwerth, L. Abrok, S. Bari, T. Buhr, M. Martins, S. Ricz, J. Viefhaus, S. Fritzsche and A. Müller, *Phys. Rev. A*, 2016, **94**, 041401.
59 S. T. Lee and K. Morokuma, *J. Am. Chem. Soc.*, 1971, **93**, 6863.
60 S. Willitsch, C. Jungen and F. Merkt, *J. Chem. Phys.*, 2006, **124**, 204312.
61 P. Hariharan and J. Pople, *Mol. Phys.*, 1974, **27**, 209.
62 L. Inhester, G. Groenhof and H. Grubmüller, *J. Chem. Phys.*, 2013, **138**, 164304.
63 O. Plekan, V. Feyer, R. Richter, M. Coreno, M. de Simone, K. C. Prince and V. Carravetta, *J. Electron Spectrosc. Relat. Phenom.*, 2007, **155**, 47.